Anal. Bioanal. Electrochem., Vol. 17, No. 9, 2025, 803-823
https://www.doi.org/10.22034/abec.2025.738932

Analytical & Bioanalytical Electrochemistry

Full Paper

Duplex Coatings of Nanoplates $ZnAl_2O_4$ on γ-Al_2O_3 for Improved Corrosion Resistance of Aluminum in Marine Environment

Nawal Boukmouche,[1,2,*] Lamia Bouchama,[3,4,5] and Rachid Benghanem[6]

[1]*Laboratory of the Interactions Materials-Environment (LIME), Jijel University, Jijel 18000, Algeria*
[2]*Faculty of Mechanical Engineering and Process Engineering, Department of Chemical and Cryogenic Engineering, University of Science and Technology Houari Boumediene (USTHB), Algiers, Algeria*
[3]*Faculty of Technology, Department of Renewable Energy, Blida 1 University, Algeria*
[4]*Laboratory of Energy Processes and Nanotechnology, Faculty of Sciences, Blida 1 University, Algeria*
[5]*Chemical Engineering Laboratory, Department of Industrial Chemistry, Blida 1 University, Algeria*
[6]*Faculty of Mechanical Engineering and Process Engineering, Department of Materials Science, University of Science and Technology Houari Boumediene (USTHB), Algiers, Algeria*

*Corresponding Author, Tel.: +213778828562
E-Mail: nawboukmouche@yahoo.com

Received: 21 August 2025 / Received in revised form: 20 December 2025 / Accepted: 27 December 2025 / Published online: 31 December 2025

Abstract- The improvement of anticorrosion properties in hybrid structures is currently a promising area of research due to their potential for multifunctional applications. This paper evaluates the corrosion behavior of ZnAl2O4/γ-Al_2O_3 duplex coatings, which were created by electrodepositing a nanostructured ZnO thin film onto nanoporous anodic alumina (AAO). The AAO was synthesized using two electrochemical anodization processes: single-step anodizing (SSA) and two-step anodizing (TSA). $ZnAl_2O_4$ was produced using an applied electric field of (-1.5 V). Potentiodynamic polarization and electrochemical impedance spectroscopy (EIS) were employed to evaluate the corrosion behavior in a 3.5 wt.% NaCl solution.The successful deposition of zinc aluminate on AAO was confirmed through additional characterization techniques included X-ray diffraction (XRD), energy-dispersive X-ray spectroscopy (EDX), scanning electron microscopy (SEM), and glow discharge optical emission spectroscopy (GDOES). scanning electron microscopy observations revealed a uniform network of $ZnAl_2O_4$nanoplates on the AAO substrate. Regarding corrosion properties, the measurements show that the $ZnAl_2O_4$/γ-Al_2O_3 coatings produced through the TSA process achieve a polarization resistance of 650 kΩ.cm^2, compared to 95 kΩ.cm^2 for those prepared by the SSA method. Overall, these findings suggest that $ZnAl_2O_4$/γ-Al_2O_3 duplex coatings have excellent potential as corrosion-resistant coatings for advanced applications.

Keywords- Anodic alumina; Chronoamperometry; Corrosion; Electrodeposition; $ZnAl_2O_4$ nanosheets

1. INTRODUCTION

Marine equipment, including ship hulls, oil platforms, pipelines, gears, and bearings, is a crucial aspect of marine engineering [1]. However, these components are prone to significant damage due to corrosion caused by the high salinity of seawater. This corrosion can lead to reduced efficiency, increased maintenance requirements, and a shorter service life for the equipment. As a result, the economic losses can be substantial, and unexpected disasters may occur [2,3]. Therefore, it is essential to enhance the durability and stability of these structures in marine environments to ensure the safety, longevity, and efficiency of maritime operations [1].

An effective approach to address this issue involves the use of suitable materials and surface engineering techniques. In particular, surface coating technologies can enhance hardness, wear resistance, and corrosion resistance without adversely affecting the properties of the underlying materials [4].

Multilayer coating systems have recently attracted considerable attention because of their outstanding properties, such as enhanced hardness, improved corrosion resistance, and better adhesion to substrates compared to monolayer coatings. These systems are also more controllable, which allows for easy development of coatings tailored to specific application requirements. Additionally, this advantageous duplex coating can save costs by reducing maintenance expenses and lowering replacement costs, as it enhances durability and longevity across a wide range of engineering materials by combining two distinct coating layers [5,6].

Research efforts have concentrated on developing duplex coatings for maritime materials that provide superior corrosion protection through hybrid deposition techniques. Recent studies have highlighted the importance of multilayers created using methods such as PVD/CVD, PVD/PECVD, PVD/ALD, and anodizing/sol-gel, owing to their improved mechanical properties and enhanced ability to mitigate corrosion damage [1,7-11]. Nevertheless, thin films fabricated by PVD or CVD frequently suffer from structural defects that compromise their protective efficiency.

During PVD processes, for example, the transfer of vapor flux can lead to issues such as pinholes, droplets, and other defects present in the deposited films. Additionally, these coatings tend to have a columnar structure, which weakens their insulating capabilities; the grain boundaries can allow electrolyte penetration into the substrate, adversely affecting both corrosion resistance and toughness [8,12,13]. PVD techniques also have limitations in terms of material choices and their line-of-sight deposition nature, making it difficult to coat the back and sides of objects, especially those with complex geometries. CVD processes generally require high temperatures (above 500°C), which can pose challenges for certain substrates or

materials [14-16]. ALD coatings are not without defects either, which can include pinholes, point defects, and line defects because of the chemical structure of the precursors and the randomness of surface reactions. Additionally, ALD deposition has a slower deposition rate compared to PVD and CVD, restricting its application in various technological fields [17]. According to studies by Panel et al. [18], the effectiveness and reliability of films used as protective layers are often limited by their mechanical properties. As a result, ALD coatings can be easily damaged under shock loading in practical applications. The performance and durability of these films are strongly governed by their adhesion strength and fracture toughness, which are critical parameters in many applications.

Unlike the methods mentioned previously, anodizing produces a thick oxide layer on metal surfaces, providing both corrosion resistance and enhanced adhesion. Coatings generated through this process protect the underlying substrate and offer benefits comparable to conventional hard coatings.

Anodic coatings formed on metals including aluminum, magnesium, and zinc generally exhibit a porous structure [19]. These micropores contribute to the reduction of residual stresses and promote mechanical interconnectivity, thereby strengthening adhesion. Nevertheless, the inherent porosity of anodized layers leads to an increased effective surface area, thereby diminishing corrosion resistance by enabling corrosive species to permeate the coating [19]. Therefore, it is crucial to achieve a well-coated, continuous, and highly adhesive film to enhance both the electrochemical and mechanical properties of materials effectively [20].

In this context, combining anodizing and electrodeposition, particularly for aluminum, significantly enhances the material's properties and functionalities. Anodizing creates a protective oxide layer on the metal surface, while electrodeposition allows for the incorporation of additional materials into this surface. This results in a composite structure with tailored performance characteristics. This method not only improves adhesion and corrosion resistance but also enables the development of innovative optical or catalytic materials. The novelty of the proposed duplex coating method lies in its unique two-step surface modification technique, which integrates anodization and electrodeposition. This strategy integrates the corrosion-protective characteristics of the anodized layer with the bioactivity of the surface layer, thereby improving both degradation resistance and the metal’s biological performance. By creating a multifunctional surface, this duplex coating surpasses traditional single-layer coatings [19]. In addition to these benefits, electrodeposition is a straightforward and effective technique for producing high-quality films suitable for various applications. The required equipment is inexpensive and does not need a vacuum, and the precursors can remain usable for several months without deterioration, unlike other methods [21]. Besides being convenient for large-area substrates, electrodeposition is also appealing for its compatibility with cost-effective substrates. It operates at a lower growth temperature compared with conventional high-temperature vacuum deposition techniques and provides fine control over film morphology,

composition, and thickness by tuning electrical parameters (current density and electrode voltage) and electrolyte composition [21].

Nanostructured metal oxides have garnered significant attention due to their unique structural properties and quantum confinement effects [22]. Recently, they have emerged as effective means to reduce corrosion. These materials typically exhibit at least one characteristic at the nanoscale (less than 100 nm), such as grain size, particle size, or structural size. One-dimensional nanomaterials include nanoparticles, nanotubes, nanowires, and nanorods, while two-dimensional nanomaterials encompass nano-platelets, nano-sheets, and nano-films [23].

In recent years, researchers in nanoscience have concentrated on developing a variety of cost-effective fabrication methods for nanomaterials and exploring their practical applications [22]. These nanostructured materials also demonstrate improved thermal, mechanical, physical, chemical, magnetic, electronic, and optical properties. Their small dimensions result in a higher surface-to-volume ratio, providing larger interfacial interaction areas. Nanocoating materials can effectively prevent corrosion by establishing a uniform physical barrier on a material's surface. Notable anti-corrosion materials for this purpose include ZrO_2, TiO_2, Al_2O_3, ZnO, SiO_2, and their composites [23, 24].

Particularly, ceramic oxide coatings, including γ-Al_2O_3 and $ZnAl_2O_4$, along with other spinel-based materials, have been shown in previous research to enhance the corrosion resistance of aluminum alloys in harsh environments, such as marine conditions. However, many published studies focus on single-layer coatings, conventional morphologies, or standalone oxide systems, which often exhibit microstructural defects that allow electrolyte penetration and limit long-term stability.

In this work, a novel duplex coating architecture is introduced for the first time, utilizing nanostructured $ZnAl_2O_4$ nanoplates as the outer functional layer and γ-Al_2O_3 as the inner barrier layer. This new coating design differs from earlier methods by combining the enhanced surface coverage, complex diffusion pathways, and chemical stability provided by $ZnAl_2O_4$ nanoplates with the high adhesion and compactness of γ-Al_2O_3. The synergistic configuration of these duplex layers improves corrosion resistance by simultaneously enhancing barrier properties and inhibiting electrolyte transport.

This study explores a novel approach that combines anodizing and electrodeposition for the treatment of aluminum surfaces. The article presents a comparative analysis of the electrochemical behavior of two multilayers developed using this innovative deposition strategy of $ZnAl_2O_4$ nanoplates on γ-Al_2O_3:SSA/electrodeposition and TSA/electrodeposition, both of which involve nanostructured ZnO on nanoporous anodized alumina.

2. EXPERIMENTAL SECTION

2.1. Synthesis and characterization

2.1.1. Preparation of substrate (AAO/Al)

High-purity aluminum (99.999% purity) substrates with an exposed area of 4 cm² were employed. Prior to anodizing, the samples were mechanically polished, degreased in acetone, and subsequently annealed at 500°C for 5 h to eliminate residual mechanical stresses and induce recrystallization of the aluminum.

Electropolishing of the aluminum surfaces was carried out using a perchloric acid–ethanol solution (1:4 by volume) under a constant applied voltage of 23 V for 2 min. Afterward, the samples were thoroughly rinsed with ethanol and dried. In the case of single-step anodized samples, aluminum anodization was carried out under potentiostatic conditions. At 23 V for a duration of 5 hours, using a 1 M sulfuric acid solution at a temperature of 3 °C. In the two-step anodizing procedure, the first anodization was conducted under the same conditions as the single-step process, followed by chemical removal of the formed oxide layer using a 0.6 M phosphoric acid bath. The second anodization was subsequently performed under identical conditions for an additional 5 h [25].

2.1.2. Preparation of $ZnAl_2O_4$ nanoplates

Initially, ZnO thin films were directly electrodeposited onto anodic aluminum oxide AAO substrates using an aqueous electrolyte containing 0.1 M zinc nitrate and 1 M potassium chloride (KCl) as the supporting electrolyte, with the pH adjusted to 6.

The ZnO films were grown at 80 °C by applying a deposition potential of −1.5 V for 180 min. A conventional three-electrode setup was employed, comprising a platinum wire as the counter electrode and a saturated calomel electrode (SCE, +0.241 V vs. SHE) as the reference.

2.1.3. Characterization techniques

The structural properties of the samples were examined using X-ray diffraction (XRD) analysis conducted on an X'Pert Pro apparatus from PANAlytical, utilizing Cu Kα radiation with a wavelength of λ = 1.5425 Å. The crystallite size of the samples was estimated using Scherrer's equation (Equation 1), applied to the peaks at 2θ = 65.78° and 45.18° for the single- and two-step anodized samples, respectively (see XRD in Figure 3):

$$d = \frac{0.9\,\lambda}{B\cos\theta} \qquad (1)$$

In this equation, (d) represents the average crystallite size (usually in nanometers**)**, λ denotes the X-ray wavelength, B corresponds to the full-width at half-maximum (FWHM) of the diffraction peak (in radians), and θ is the Bragg angle (in radians) [26]. Additionally, a Quanta 200 scanning electron microscope (SEM) was employed to investigate the microstructure and chemical composition of the samples. Glow Discharge Optical Emission Spectroscopy (GDOES) [27] using a GD Profiler 2 (Horiba/Jobin-Yvon) was employed to investigate the chemical composition and surface profiles of the $ZnAl_2O_4$/AAO/Al composite. This technique is well suited for elemental surface measurement and depth profiling of thin film materials [28].

Electrochemical measurements were executed using a conventional three-electrode electrochemical cell. This system comprised a $ZnAl_2O_4$/AAO/Al working electrode, a platinum (Pt) counter electrode, and a saturated calomel reference electrode (SCE). Electrochemical measurements were carried out in potentiostatic mode using a Radiometer Analytical Voltalab 40 PGZ301 potentiostat/galvanostat, with the working electrode having a surface area of 1 cm^2.

The electrochemical behavior of the $ZnAl_2O_4$/AAO/Al plates was assessed through Electrochemical Impedance Spectroscopy (EIS) under unstirred conditions. The specimens were immersed in a 3.5% NaCl solution at ambient temperature for time intervals of 2, 4, 6, 24, 28, and 30 h. Electrochemical impedance spectroscopy was carried out using an AC amplitude of 10 mV at the open-circuit potential, over a frequency range from 100 kHz to 1 mHz. Following 1 h of immersion, potentiodynamic polarization measurements were performed.

3. RESULTS AND DISCUSSION

3.1. Preparation of zinc oxide

To investigate the mechanism of $ZnAl_2O_4$ deposition on AAO/Al using an electrochemical technique the current–time (i–t) curves were recorded., as shown in Figure 1. Both curves indicate that $ZnAl_2O_4$ was deposited on AAO/Al at a deposition potential of −1.5 V for 180 minutes, maintained at a fixed temperature of 80 °C. Initially, the electrodeposition process led to a rapid increase in current density, which is related to double-layer charging. After approximately one hundred seconds, this increase slowed down, eventually reaching a steady-state current density of about -30 µA cm^2 after 30 minutes.

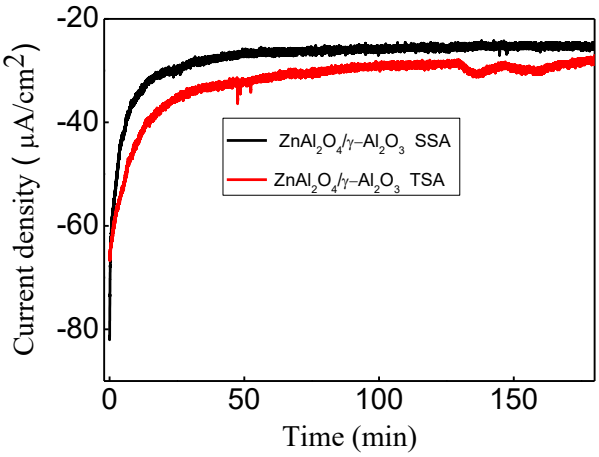

Figure 1. Chronoamperometric curves at a deposition potential of -1.5 V for the growth of $ZnAl_2O_4$ on γ-Al_2O_3 prepared by (SSA) and (TSA)

It is important to note that the cathodic current of $ZnAl_2O_4$/grown on alumina through single-step anodizing was superior to that produced by two-step anodizing. This can be attributed to the

heterogeneous morphology, which features numerous cavities that facilitate the flow of current more effectively [31]. These findings are consistent with results from previous studies [29,30].
The cathodic electrodeposition of $ZnAl_2O_4$ film on Al_2O_3/Al using zinc nitrate as a precursor was proposed, as detailed by the following chemical equations [31]:

$$Zn(NO_3)_2 \rightarrow Zn^{2+}+2NO^{3-} \quad (2)$$

$$2H_2O+2e- \rightarrow H_2+2OH^- \quad (3)$$

$$Zn^{2+}+ 2OH^- \rightarrow Zn(OH)_2 \quad (4)$$

$$Zn(OH)_2 \rightarrow ZnO+H_2O \quad (5)$$

Initially, the nitrate ions are reduced near the substrate, resulting in the formation of hydroxide ions (OH^-), which increases the local pH at the substrate. This pH control is a crucial aspect of the process. The hydroxide ions then react with the zinc ions (Zn^{2+}) to form zinc hydroxide ($Zn(OH)_2$). This compound is subsequently decomposed to yield ZnO into AAO [32].

When an electric field of -0.5 V is applied, the crystal structure of ZnO that is injected into Al_2O_3 becomes polarized, resulting in a change in its properties. The ions within the unit cell are displaced by electrostatic forces. Depending on the placement of the electric field and the orientation of the hexagonal axes, aluminum (Al) can substitute for zinc (Zn) at the Zn site. This substitution reaction, influenced by the electric field, leads to the formation of $ZnAl_2O_4$ [33], which can be described as:

$$ZnO + Al_2O_3 \rightarrow ZnAl_2O_4\,(s) \quad (6)$$

At this point (30 minutes), the growth of the $ZnAl_2O_4$ film became nearly constant and uniform, primarily due to the gradual coverage of the substrate by $ZnAl_2O_4$. In other words, upon applying the potential, the electrolyte was in direct contact with the substrate (electrode). After a short period, the electrode became entirely covered with $ZnAl_2O_4$nanoplates [22].

3.2. Structural analysis

X-ray diffraction (XRD) analysis is extensively employed to determine the crystal structure and phase composition of materials. This method allows for the determination of the crystal phase and structure of the materials being studied, as well as the size and orientation of their grains.

The typical XRD patterns of $ZnAl_2O_4$ films grown on AAO substrates, produced through SSA and TSA processes, are illustrated in Figure 2. The results indicate that $ZnAl_2O_4$ (JCPDS no. 00-005-0669) is the predominant crystallographic phase observed. The intense diffraction peaks can be accurately indexed to a face-centered cubic structure with the space group Fd-3m and lattice parameters of a = b = c = 8.08480 Å. The characteristic peaks observed at 2θ values

of 36.98°, 38.85°, 45.18°, 59.32°, 65.7°, and 78.9° correspond to the (311), (222), (400), (511), (440), and (622) diffraction planes, respectively [34,35].

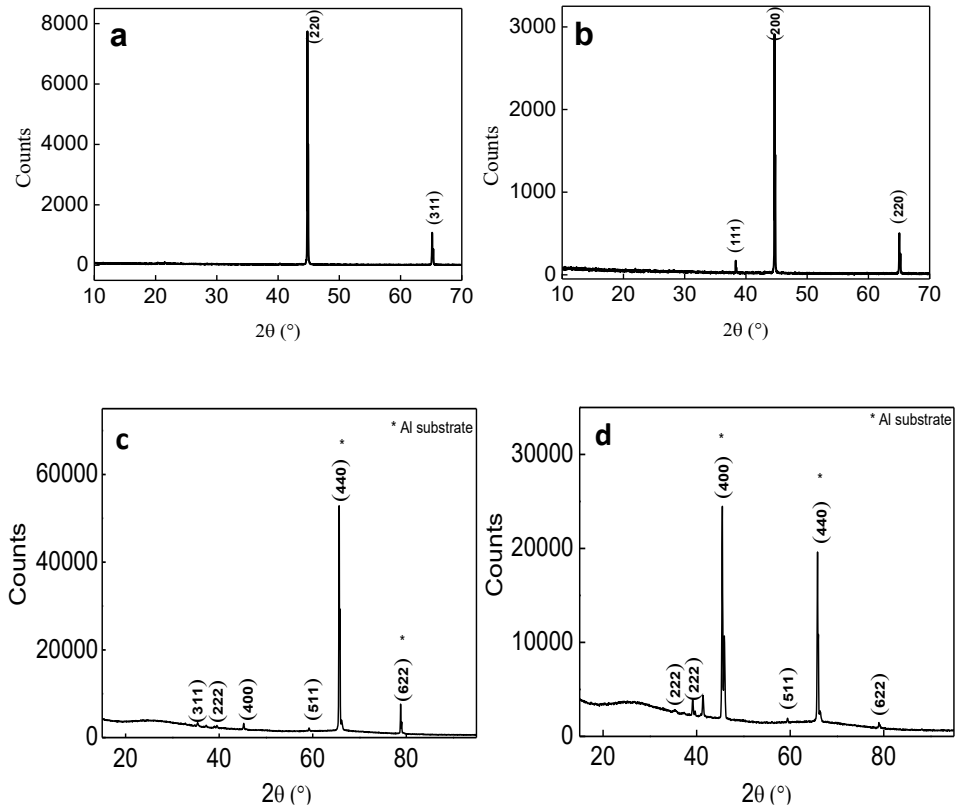

Figure 2. X-ray diffraction (XRD) patterns of AAO and $ZnAl_2O_4/\gamma$-Al_2O_3 formed by (a,c) SSA and (b,d) TSA

Additionally, XRD analysis identified a second phase as γ-Al_2O_3 (JCPDS 29-0063). The peaks observed at $2\theta = 39.15°$ and $2\theta = 45.18°$ correspond to the (222) and (400) diffraction planes, respectively. These peaks are indicative of a cubic structure characterized by the same space group Fd-3m and lattice parameters of a = b = c = 7.924 Å.

Moreover, a peak at 41.34° suggests the presence of KCl as an impurity, likely originating from the supporting electrolyte used to enhance conductivity during bath deposition. The XRD spectra confirm that only the $ZnAl_2O_4$ and γ-Al_2O_3 phases are present, indicating a significant transformation of $ZnAl_2O4$.

The produced nanoplates exhibited a tendency to align along the (440) direction for the $ZnAl_2O_4/\gamma$-Al_2O_3/Al (SSA) sample and along the (400) and (440) crystal planes, with pronounced peaks observed at approximately 45° and 65° for the $ZnAl_2O_4/\gamma$-Al_2O_3/Al (TSA) sample. The presence of these strong diffraction peaks at specific crystal planes indicates that the nanoplates possess good crystallinity.

Applying an electric field creates a force on the electric charges present in the crystal, which causes a change in the crystal structure and therefore a deformation of the material.

By applying an electric field, ZnO is effectively injected into AAO, and its properties are altered; the unit cell ions are moved by electrostatic forces. Al is simply substituted for Zn at the Zn site depending on the electric field position and the hexagonal axes [33].

The results confirmed the substitution reaction between ZnO and aluminum oxide (Al_2O_3) into $ZnAl_2O_4$ nanoplate by applying an electric field.

The results show that only a network of $ZnAl_2O_4$ nanoplates on γ-Al_2O_3 is present. Similar results have been reported in previous studies [36,37]. These compositions have been confirmed through Energy Dispersive X-ray (EDS) and Glow Discharge Optical Emission Spectroscopy (GDOES) analyses, as shown in Figures 5 and 6.

We estimated the crystallite size of the $ZnAl_2O_4$ nanoplates using the Scherrer equation, finding values of approximately 1.13 nm for the $ZnAl_2O_4$/γ-Al_2O_3 SSA sample and 12.72 nm for the $ZnAl_2O_4$/γ-Al_2O_3 TSA sample.

3.3. *Morphological analysis*

The SEM images in Figure 3 illustrate the morphology of the Anodic Aluminum Oxide (AAO) after undergoing single- and two-step anodizing processes, as well as the surface topography of $ZnAl_2O_4$ supported on γ-Al_2O_3.

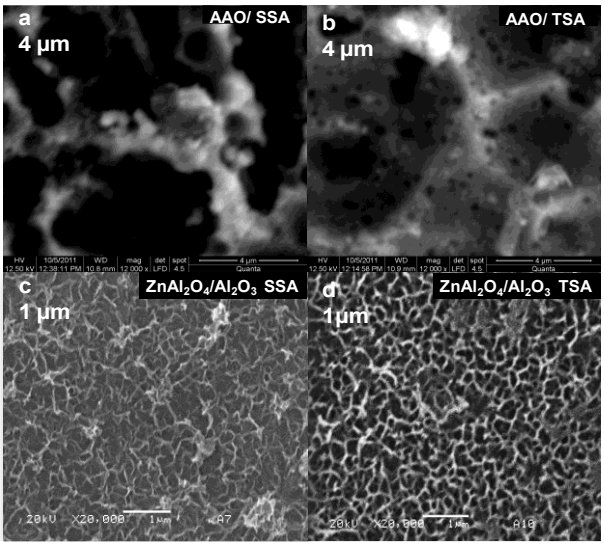

Figure 3. Scanning electron microscopy (SEM) micrographs of samples(a) AAO/SSA, (b) AAO/TSA, (c) $ZnAl_2O_4$/γ-Al_2O_3//SSA and (d) $ZnAl_2O_4$/γ-Al_2O_3//TSA

The anodic films produced through the two different processes exhibit distinct surface morphologies. The AAO surface features numerous micropores of varying shapes and sizes arranged randomly. In contrast, the anodic films created using the TSA process display a smoother surface that is less porous, characterized by smaller diameter pores. In the case of anodic films produced via the SSA approach (see Figure 3a), a heterogeneous distribution of

larger holes can be observed. This irregularity arises from field-assisted oxide dissolution [38]. Consequently, the surface is marked by many craters, each measuring just a few microns across. According to Patermarakis et al. [39], this phenomenon can be attributed to the local interconnection of pore openings, resulting in the formation of these small craters.

The morphology of $ZnAl_2O_4$ supported on γ-Al_2O_3 appears similar, as shown in Figure 3 (c, d). Examination of the surface films reveals that a porous network of $ZnAl_2O_4$ nanoplates is uniformly distributed across the alumina supports. In Figure 3a, the nanoplates tend to aggregate randomly over a surface that has already been coated with nanoplaets. This aggregation may occur near micropores or crater-like areas and can be attributed to the numerous defects present on the anodic aluminum oxide (AAO) substrate [26]. Furthermore, Figure 3b indicates that the texture and morphology of the nanoplates deposited on γ-Al_2O_3 using the TSA process are more orderly compared to those produced by the SSA process. The degree of $ZnAl_2O_4$ aggregation is lower due to the reduced number of random distributions of the discharged micropores. This structured arrangement has also been observed in previous studies [40]. Additionally, Ahmad Umar et al. [41] reported a similar microstructure of ZnO nanosheet networks grown on silicon substrates.

3.4. Elemental analysis

The composition of elements and the existing mineral phases can be identified using Energy Dispersive Spectroscopy (EDS) analysis. Figure 4 displays representative EDS spectra of $ZnAl_2O_4$ nanoplates deposited on alumina substrates, obtained through TSA approach. The EDS spectra illustrate the main peaks corresponding to Zn, O, and Al. This presence is attributed to the formation of $ZnAl_2O_4$ nanoplates on alumina supports, with the Al and O peaks arising from the anodic alumina layer used as the substrate.

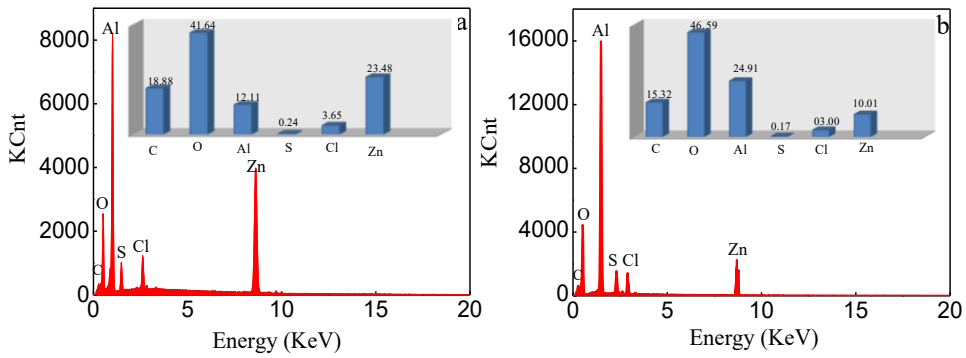

Figure 4. EDS spectrum of $ZnAl_2O_4$/γ-Al_2O_3 coatings obtained via (a) single-step anodizing (SSA) and (b) two-step anodizing (TSA)

Additionally, we observe weak peaks representing several other elements, including S, Cl, and C. The detected sulfur (S) is likely derived from sulfuric acid, which can become embedded

within the alumina layer. It is well-known that porous films generated in sulfuric acid are often susceptible to contamination by acid-derived species, particularly sulfate (SO_4^{2-}) [42]. The detection of chlorine (Cl) suggests a significant penetration of Cl anions into the $ZnAl_2O_4$ film, which may originate from the supporting electrolyte (KCl) used during electrodeposition of ZnO in AAO. The higher levels of carbon (C) can be attributed to the use of graphite glue during the EDS/SEM analysis [25]. From the EDS results, the approximate atomic ratios of Zn/Al/O in both cases are 1:2:4, which proves that $ZnAl_2O_4$ is effectively synthesized under this condition.

3.5. Glow discharge optical emission spectrometry (GDOES)

A GDOES depth profile for $ZnAl_2O_4$ grown on an alumina substrate is presented in Figure 5. The curves depict the weight percentage of $ZnAl_2O_4$ in relation to the depth of the composite film. The anodic films are primarily composed of aluminum (Al) and oxygen (O), while sulfur (S) is present in smaller amounts and is considered a contaminant from the electrolytic species [42].

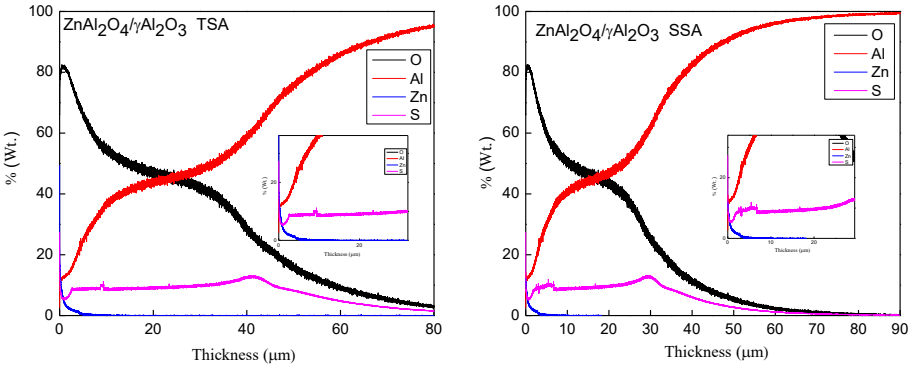

Figure 5. (GDOES) spectra of $ZnAl_2O_4/\gamma$-Al_2O_3

The GDOES analysis indicates a high oxygen content, which is expected due to the formation of aluminum oxide (Al_2O_3) and $ZnAl_2O_4$ from the combination of aluminum and zinc. The oxygen content decreases gradually with depth. In the dual oxide film, the distributions of aluminum (Al) and oxygen (O) differ between the two layers: in the porous layer, their distribution is uniform, while in the barrier layer, the amount of Al increases and the amount of O decreases.

The estimated thicknesses of the dual oxide films for the TSA and SSA processes were 24.10 μm and 18.50 μm, respectively. Additionally, only little amounts of zinc (Zn) were detected at the surface of the alumina, and this concentration decreases gradually with the depth of the alumina. This finding reflects the incorporation of Zn into the anodic aluminum oxide (AAO), confirming the formation of a thin layer of $ZnAl_2O_4$, measuring just a few micrometers, on top of the Al_2O_3 surface. The estimated thicknesses of the $ZnAl_2O_4$ thin films on γ-Al_2O_3 for

the TSA and SSA processes were 4.00 µm and 3.08 µm, respectively. There is a slight difference in thickness, although their electrodeposition was carried out under the same conditions. This difference in the thickness of the $ZnAl_2O_4$ film can be explained by the difference in pore diameter of AAO pores. In the case of SSA, the diameter is in the micropore range, while in the case of TSA, the diameter is finer. This also reflects the pore depth in both cases, 4.00 and 3.08 for the TSA and SSA samples, respectively.

3.6. Corrosion resistance

We have developed a new supported coating based on $ZnAl_2O_4$ on a γ-Al_2O_3 substrate to enhance its anticorrosion properties. To evaluate its long-term effectiveness and corrosion resistance, the coating must be tested in an aggressive environment. We used electrochemical impedance spectroscopy and potentiodynamic polarization to study the resistance of $ZnAl_2O_4$/γ-Al_2O_3 electrodes.

3.6.1. Impedance spectra of $ZnAl_2O_4$/γ-Al_2O_3

The obtained Nyquist plots and the corresponding equivalent circuit model are illustrated in Figure 6.

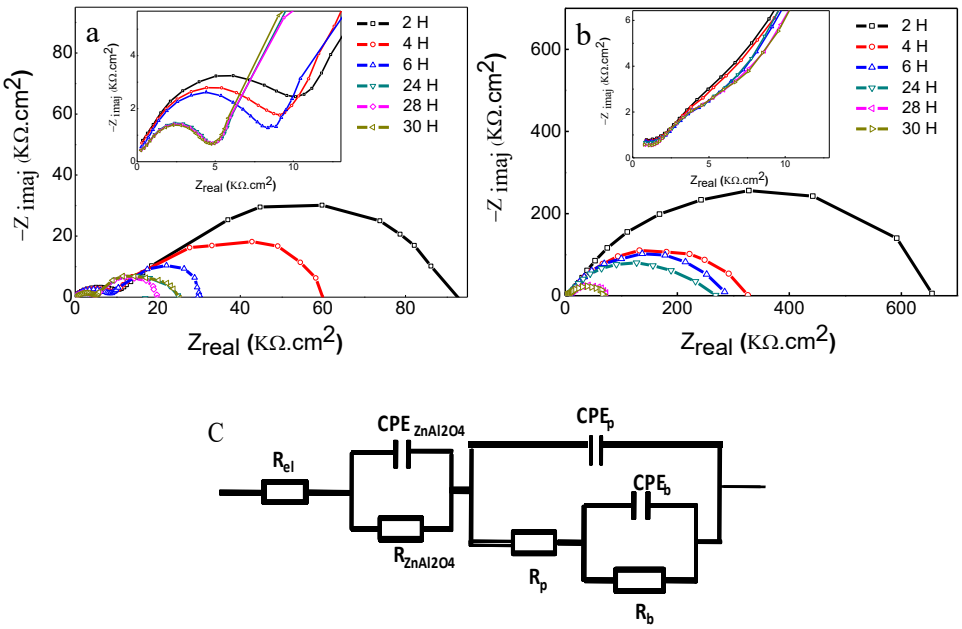

Figure 6. Nyquist plots as a function of immersion time in a 3.5% NaCl solution at 25°C for $ZnAl_2O_4$/γ-Al_2O_3 prepared by (a) SSA, (b) TSA, and (c) equivalent circuit models of ZnO/AAO/Al

The Nyquist plots reveal three distinct capacitive loops. It is evident from Figure 6 that the curve shapes for $ZnAl_2O_4$/γ-Al_2O_3 differ significantly between the two cases presented. Figure 6(a) displays a loop at high-frequency and two overlapping loops at medium and low

frequencies. The high-frequency range is attributed to the characteristics of the $ZnAl_2O_4$ nanoplates, while the medium and low frequencies ranges correspond to the properties of the porous and barrier layers, respectively [43-47]. In contrast, Figure 6(b) shows that the three capacitive loops merge into a single loop of $ZnAl_2O_4$ nanoplates on γ-Al_2O_3. Notably, the thickness of the anodic alumina layer was measured using the GDOES depth profile, as depicted in Figure 5. The measurement results indicated that the single-step anodized sample had a thin coating at approximately 18.5 μm, while the two-step anodized sample exhibited an even thicker coating at around 24.10 μm.

The thicker $ZnAl_2O_4$ nanoplate film produced on γ-Al_2O_3 through TSA have an average thickness of 4.00 μm, compared to 3.08 μm for the $ZnAl_2O_4$/γ-Al_2O_3/SSA. Furthermore, the substitution reaction between ZnO and aluminum oxide (Al_2O_3) into $ZnAl_2O_4$ nanoplate by applying an electric field lead to sealing of nanoporous alumina with $ZnAl_2O_4$, leading to a denser and more protective coating. The larger loops were produced by the $ZnAl_2O_4$/γ-Al_2O_3 samples created through a two-step anodizing process, while a smaller semicircle was observed in the samples prepared using a single-step anodizing process. The larger diameter of the semicircles in the sample provides better protection against corrosion effects, based on a previous study [23].

As shown in Figure 6, the polarization resistance (R_p) values (Table 1) are higher for the $ZnAl_2O_4$/γ-Al_2O_3 samples produced via two-step anodizing compared to those made through single-step anodizing. This indicates that the $ZnAl_2O_4$/γ-Al_2O_3 created with the two-step anodizing method exhibits greater corrosion resistance than the one produced with the single-step method.

Additionally, Figure 6 demonstrates a significant reduction in the diameter of the capacitive loops at low frequencies as immersion time increases until 24 hours. This observation can be correlated with the decrease in the polarization resistance of the duplex coatings, which gradually degrade due to the penetration and migration of chloride ions (Cl^-) through the heterogeneous structure, which includes micropores, craters, and grain boundaries of the $ZnAl_2O_4$ nanoplate to the γ-Al_2O_3 coating [25].

After this duration (Figure 7), two distinct behaviors are observed in duplex coatings. In the case of the two-step anodized sample, we notice at 28 and 30 hours the superposition of two capacitive loops, indicating stable resistance polarization after 28 hours of immersion. In contrast, for the single-step anodized sample, the capacitive loop at 30 hours exhibits an increase while maintaining the same value of polarization resistance (R_p) as at 24 hours.

The slow decrease and stability after 28 h in resistance (R_p) can be attributed to the $ZnAl_2O_4$ nanoplates that are coated and embedded within the pores of the alumina. These nanoplates help to inhibit the dissolution of alumina, thereby enhancing its corrosion resistance. $ZnAl_2O_4$ is known for its excellent corrosion resistance [48].

The slow decrease and stability after 28 h in resistance (R_p) (Figure 7) can be attributed to the $ZnAl_2O_4$ nanoplates that are coated and embedded within the pores of the alumina. These nanoplates help to inhibit the dissolution of alumina, thereby enhancing its corrosion resistance. $ZnAl_2O_4$ is known for its excellent corrosion resistance.

Furthermore, $ZnAl_2O_4$ nanoplates form on the surface of alumina, creating a physical barrier that prevents aggressive agents (such as chlorides, sulfates, or oxygen) from reaching the underlying substrate. This suggests that the alumina layer remains intact, attributed to the film's effective protection that inhibits electrolyte penetration

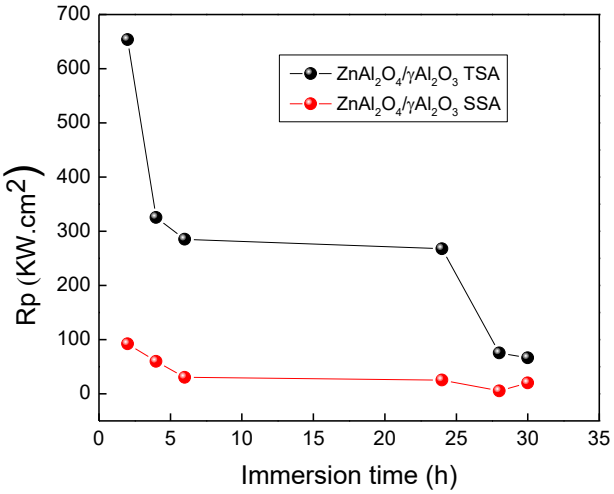

Figure 7. Polarization resistance (R_p) evolution versus immersion time for $ZnAl_2O_4$/γ-Al_2O_3 coatings obtained by SSA and TSA

On the other hand, the stability and increase of R_p over immersion time may also be explained by a self-sealing phenomenon. As the porous layer of alumina absorbs water, leading to its hydration, it transforms into voluminous hydrated alumina, which facilitates self-sealing. Consequently, the porous layer becomes more robust [25].

3.6.1.1. Electrical equivalent circuit

EIS data were fitted with the equivalent circuit model using ZView software. Figure 6c illustrates the proposed equivalent circuit (EC) model. The EC provided the best fit to the impedance data. SSA and TSA approaches both showed similar CEs. It is evident from SEM images and GDOES analysis that the primary difference between samples developed with $ZnAl_2O_4$/γ-Al_2O_3/SSA and $ZnAl_2O_4$/γ-Al_2O_3/TSA lies in their microstructure and duplex coating thickness.

The $ZnAl_2O_4$/γ-Al_2O_3/TSA sample has an orderly organization and a less porous structure, whereas the SSA has an irregular distribution with many craters. The model comprises three sections arranged in series, beginning with the resistance of the electrolytes (R_{el}). The second

section of the circuit is characterized by a parallel combination of a constant phase element ($CPE_{ZnAl2O4}$) and a resistance ($R_{ZnAl2O4}$), which represents the $ZnAl_2O_4$ nanoplate film.

In the third part, two parallel branches were combined. The first branch represents the porous layer, characterized by a constant phase element (CPE_p) and a resistance (R_p). The second branch represents the barrier layer, characterized by a constant phase element (CPE_b) and a resistance (R_b). This circuit consists of the following components: R_{el} represents the electrolyte resistance between the coating surface and the referencing electrode. In NaCl solution, R_{el} is insignificant. $R_{ZnAl2O4}$: The resistance of the $ZnAl_2O_4$ films, which is determined by the conductivity of the electrolyte in the film pores. $CPE_{ZnAl_2O_4}$: constant phase element, accounting for irregularities, non-ideal capacitance, and variations in the properties of the $ZnAl_2O_4$ film. R_p: The resistance of the porous layer is determined by the electrolyte conductivity within its porosity. The Constant Phase Element (CPE_p) accounts for irregularities, non-ideal capacitance, and variations in the properties of the films [25]. The barrier is defined by its resistance (R_b) and the (CPE_b) of the barrier layer. The impedance of the CPE is calculated as follows:

$$CPE = \frac{1}{(2\pi JfC)^{\alpha}} \qquad (7)$$

where, α_p and α_β represent the deviation from ideal capacitive behavior and are associated with CPE_p and CPE_β, respectively [49].

Table 1 summarizes the parameters obtained by fitting the experimental impedance spectra of $ZnAl_2O_4$/ γ-Al_2O_3.

Table 1. Adjustment of stimulation parameters for EIS spectra of $ZnAl_2O_4$/γ-Al_2O_3 in 3.5% NaCl medium

				Two-step anodizing										Single-step anodizing						
Immersion time(h)	**R_{el} (Ω.cm^2)**	**$R_{ZnAl2O4}$(Ω.cm^2)**	**$\alpha_{ZnAl2O4}$**	$CPE_{ZnAl2O4}$ (Ω^{-1}.cm^{-2}.s$^{\alpha}$)	**R_p(Ω.cm^2)**	**α_p**	CPE_p (Ω^{-1}.cm^{-2}.s$^{\alpha}$)	**R_b (Ω.cm^2)**	**α_b**	CPE_b (Ω^{-1}.cm^{-2}.s$^{\alpha}$)	**R_{el} (Ω.cm^2)**	**$R_{ZnAl2O4}$(Ω.cm^2)**	**$\alpha_{ZnAl2O4}$**	$CPE_{ZnAl2O4}$ (Ω^{-1}.cm^{-2}.s$^{\alpha}$)	**R_p (Ω.cm^2)**	**α_p**	CPE_p (Ω^{-1}.cm^{-2}.s$^{\alpha}$)	**R_b (Ω.cm^2)**	**α_b**	CPE_b (Ω^{-1}.cm^{-2}.s$^{\alpha}$)
2	0.01	3.11 E13	1.0	3,75 E-9	3.09 E16	1.0	2,36 E-11	3.08 E4	0.79	7,38 E2	2.16 E2	1.72 E4	0.45	3,33 E-6	6.39 E5	1.00	2,66 E-9	7.59 E2	0.82	1,06 E-6
4	3.79E -7	8.48 E5	0.71	1,02 E-7	1.22 E15	0.75	1,18 E7	4.10 E4	0.72	8,99 E-6	4.17 E2	3.03 E5	0.79	1,42 E-6	1.16 E4	1.00	1,23 E-9	1.40 E3	0.55	1,44 E-6
6	9.99E -3	4.81 E5	1.0	1,13 E-5	2.61 E5	0.74	1,39 E-5	8.44 E3	0.69	1,38 E-7	4.05 E2	2.58 E5	0.81	1,87 E-6	1.06 E4	1.00	1,22 E-9	1.31 E3	0.53	1,74 E-6
24	9.99E -3	8.78 E3	0.7	3,41 E-5	9.25 E4	1.00	2,32 E-5	4.93 E3	0.65	2,95 E-7	3.93 E2	1.37 E3	0.55	2,32 E-6	6.76 E4	1.00	2,63 E-9	7.51 E2	0.79	3,61 E-6
28	9.86E -2	8.89 E3	0.64	3,13 E-7	6.76 E4	0.86	2,56 E-5	4.94 E2	0.98	9,63 E-6	4.02 E2	4.13 E3	0.56	2,19 E-6	2.81 E4	1.00	2,63 E-9	7.58 E2	0.78	3,64 E-6
30	1.04E -3	5.26 E4	0.92	2,70 E-5	3.86 E4	0.80	1,78 E-5	4.72 E3	0.65	2,83 E-7	3.55 E2	2.19 E4	0.85	3,58 E-6	1.05 E4	1.00	1,40 E-9	1.03 E3	0.54	2,26 E-6

3.6.2. Dynamic potential polarization

Figure 8 presents the polarization curves of electrodeposited $ZnAl_2O_4$ on alumina, obtained through single and two anodizing processes. The corrosion current density ($i_{(corr)}$) was obtained from the extrapolation of the anodic and cathodic Tafel slopes to the corrosion potential ($E_{(corr)}$) [49]. The polarization resistance (R_p) was evaluated using the relationship described in Ref. [7].

$$R_p = \frac{\beta a\ \beta c}{2.03 icorr\ (\beta a + \beta c)} \qquad (8)$$

Where β_a and βc represent the inverse slopes of the anodic and cathodic branches, respectively, and $J_{(corr)}$ corresponds to the corrosion current density.

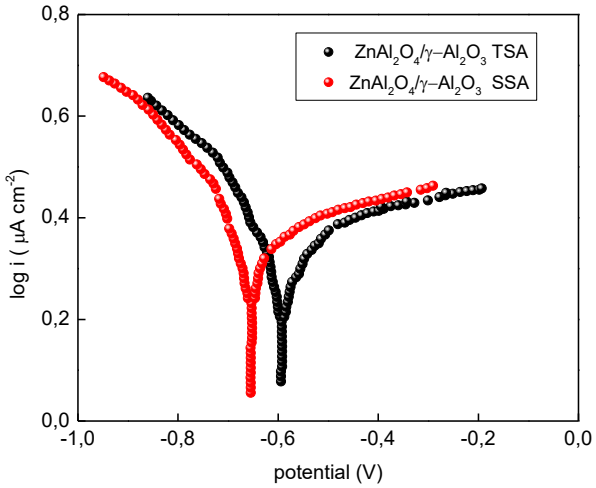

Figure 8. Potentiodynamic polarization curves of $ZnAl_2O_4/\gamma$-Al_2O_3 formed by (a) SSA and (b) TSA in a 3.5% NaCl medium, 1 hour after immersion at 25°C

Table 2. Corrosion parameters of $ZnAl_2O_4/\gamma$-Al_2O_3 formed by SSA and TSA

	E_{corr} (V)	R_p (KΩ. cm^2)	i_{corr} (nA.cm^{-2})	βc	βa
TSA	-0.580	650.000	0.290	|-50.700|	0.355
SSA	-0.645	93.380	0.314	|-55.700|	11.140

The polarization curves of the coated samples show slight differences; however, for the TSA coatings, both the cathodic and anodic branches exhibit lower current density values, while their corrosion potential is observed to be more positive. The corrosion potentials for the $ZnAl_2O_4/\gamma$-Al_2O_3/TSA and $ZnAl_2O_4/\gamma$-Al_2O_3/SSA coatings are -0.580 V and -0.645 V (*vs.* SCE), respectively (see Table 2).

The $ZnAl_2O_4/\gamma$-Al_2O_3/TSA coating exhibits a marked reduction in corrosion current density (0.290 $nA \cdot cm^{-2}$) compared to the $ZnAl_2O_4/\gamma$-Al_2O_3/SSA sample, which shows an $i_{(corr)}$ value of 0.314 $nA \cdot cm^{-2}$.

In agreement with the EIS results, a significantly high polarization resistance (R_p) of 650.00 $k\Omega \cdot cm^2$ was obtained after 1 h of immersion in NaCl solution, which is approximately six times higher than that of the SSA coating (93.38 $k\Omega \cdot cm^2$).

Duplex coatings improve corrosion protection by shifting the corrosion potential toward more noble values and reducing the corrosion current density. The $ZnAl_2O_4/\gamma$-Al_2O_3 coating fabricated via the TSA approach exhibited enhanced corrosion resistance, as evidenced by a higher $E_{(corr)}$ and a lower $i_{(corr)}$.

The thicker alumina film coated with $ZnAl_2O_4$ nanoplates likely acts as an effective physical barrier, thereby enhancing corrosion resistance. The thickness of the duplex coating plays a crucial role in reducing the corrosion susceptibility of the substrate. This improvement can also be attributed to the high density and uniform distribution of $ZnAl_2O_4$ nanoplates adhered to the alumina layer, which hinder chloride ion penetration.

In contrast, the sample prepared using the single-step anodizing process displays a non-uniform distribution of $ZnAl_2O_4$ nanoplates and aggregates on the surface of the alumina. Additionally, the alumina layer exhibits high porosity and numerous surface cracks, which allow chloride ions to penetrate through the duplex coating, ultimately compromising its corrosion resistance.

Furthermore, Tianyu Zhang et al. [50] investigated the influence of $ZnSO_4$ concentration on the corrosion behaviour of Al_2O_3/ZnO composite coatings formed in situ via plasma electrolytic oxidation (PEO) on aluminium alloy substrates. Their results demonstrated a proportional relationship between $ZnSO_4$ concentration and the thickness and density of the PEO coating, leading to enhanced corrosion resistance. The optimal PEO coating exhibited the highest corrosion resistance, through a corrosion current density of 4.457×10^{-9} $A \cdot cm^{-2}$.

In a recent study by Weiwei He et al. [51], a multifunctional coating of ZnO on anodic aluminum oxide-zinc was developed in order to improve corrosion resistance and antibacterial properties. Coated samples were isothermally heat treated at 150, 250, and 350°C, respectively. The study showed that the AZ-250 sample had the lowest corrosion current density (1.127×10^{-8} $A \cdot cm^{-2}$) and the highest charge-transfer resistance (4.65×10^5 $\Omega \cdot cm^2$) compared to the AZ-150 and AZ-350 samples.

A comparison of the results from this study with recent research confirms that the duplex coating $ZnAl_2O_4$, developed through the electrodeposition of ZnO in anodic aluminum oxide (AAO), greatly improves the corrosion resistance of aluminum. The enhancement is particularly significant in the $ZnAl_2O_4/Al_2O_3$ samples prepared using the two-step anodizing technique. As a result, this material is suitable for a wide range of antibacterial applications,

including heat exchangers, medical instrument casings, transport structures, and especially marine constructions.

4. CONCLUSION

This study aims to improve aluminum corrosion resistance through a novel duplex coating of $ZnAl_2O_4/\gamma\text{-}Al_2O_3$ synthesized using anodizing/electrodeposition. Firstly, ZnO was synthesized by electrodeposition using ($Zn(NO_3)_2$) as source material on AAO substrates. AAO was generated via single- and two-step anodizing methods. The detailed structural characterization revealed that only the ($ZnAl_2O_4$) structure with a face-centered cubic phase was obtained by substitution reaction between ZnO and aluminum oxide (Al_2O_3) into $ZnAl_2O_4$ nanoplate by applying an electric field, as confirmed by other analyses, such as EDS. SEM analysis revealed a homogeneous and regular nanoplate network grown on an alumina substrate in both samples. Particularly, the $ZnAl_2O_4/\gamma\text{-}Al_2O_3$/SSA sample presents aggregates dispersed alternately on the crater's surface. GDOES analysis of $ZnAl_2O_4/\gamma\text{-}Al_2O_3$ indicates that skinny films are incorporated into the pores as well as deposited on the alumina surface. The corrosion resistance of nanoplates $ZnAl_2O_4/\gamma\text{-}Al_2O_3$ was studied by EIS and dynamic potential polarization. EIS characterization showed that nanoplates of $ZnAl_2O_4$ supported on alumina developed through a TSA process demonstrate greatly improved corrosion resistance, correlated with the thickness of both the $ZnAl_2O_4/\gamma\text{-}Al_2O_3$ duplex coating and the $ZnAl_2O_4$ nanoplates, the thickest coating (about 24.8 µm $ZnAl_2O_4$ nanoplates) and (4.00 µm $ZnAl_2O_4$). Additionally, this finding was correlated with the microstructure of the duplex coating, characterized by a denser and more homogeneous morphology of $ZnAl_2O_4$ nanoplates, as well as a less porous surface of alumina.

Acknowledgments

The authors gratefully acknowledge the grant support by the laboratory LIME and the Department of Chemical and Cryogenic Engineering, University of Science and Technology Houari Boumediene (USTHB), Algiers, Algeria. The authors also express their thanks to reviewers and the associate editor for their helpful comments.

Declarations of interest

The authors declare no conflict of interest in this reported work.

REFERENCES

[1] E. Kaady, S. Sayegh, M. Bechelany, R. Habchi, and A. Alhussein, Coating 13 (2023) 1017.

[2] B. Jean-Denis, Revêtements nanostructurés pour la protection des métaux dans les environnements marins, Doctoral theses, University of Quebec at Chicoutimi (2016).
[3] D.H. Xiaa, C. M. Denga, D. Macdonaldc, S. Jamalid, D. Millse, J.L. Luof, Michael G. Streblg, M. Amirih, W. Jini, S. Songa, and W. Hu, J. Mater. Sci. Techno. 112 (2022) 151
[4] R. Fathi, H. Wei, B. Saleh, N. Radhika, J. Jiang, A. Ma, M. H. Ahmed, Q. Li, and K.K. Ostrikov, Appl. Mater. Today 26 (2022) 101373.
[5] C. Liu, H. Ju, P. Han, C. Quan, C. Mo, Y. Zhao, Y. Geng, J. Xu, and L. Yu, Vacuum 178 (2020) 109368.
[6] M. Sathish, N. Radhika, and B. Saleh, Met. Mater. Int. 29 (2023) 1229.
[7] E. Kaady, A. Alhussein, M. Bechelany, and R. Habchi, Thin Solid Films. 759 (2022) 139476.
[8] M. Monika Szindler, M. Szindler, J. Bicz, and K. Matus, Coating 15 (2025) 436.
[9] E. Kaady, R. Habchi, M. Bechelany, E. Zgheib, and A. Alhussein, Coating 13 (2023) 65
[10] D. Osorio, J. López, H. Tiznado, M.H. Farías, M.A. Hernández-Landaverde, M. Ramírez-Cardona, J. M. Yáñez-Limón, J.O. Gutiérrez, J.C. Caicedo, and G. Zambrano, Crystallography 10 (2020) 620.
[11] J. Chen, Z. He, and Y. Wang, Chem. Eng. J. 497 (2024) 154414.
[13] P. Panjan, A. Drnovšek, P. Gselman, M. Cekada, and M. Panjan, Coating 10 (2020) 447.
[12] P. Panjan, A. Drnovšek, P. Gselman, M. Cekada, M. Panjan, T. Bonˇcina, and D. KekMerl, Coating 9 (2019) 511.
[14] X. R. Wang, and G. Yushin, Energy Environ. Sci. 8 (2015) 1889.
[15] B. Uzakbaiuly, A. Mukanova, Y. G. Zhang, and Z. Bakenov, Front. Energy Res. 9 (2021) 625123.
[16] K. V. Carballo, M. Singh, and X. Meng, Chem. Commun. 61 (2025) 1574.
[17] P. C. Yun Na, C. J. No, B. Lim, and S. M. Cho, Vacuum 236 (2025) 114154.
[18] J. N. Ding, X.F. Wang, N.Y. Yuan, C.L. Li, Y.Y. Zhu, and B. Kan, Surf. Coat. Tech. 205 (2011) 2846.
[19] V.S. Simi, V.S. Vineeth, S. Arun Kumar, and A. Srinivasan, Mater. Chem. Phys. 343 (2025) 131066.
[20] D. Tulus, L. Tobing, B. Prakoso, C. Gustine Adios, N.H. Hawari, R. Erlangga M. Wiriadinata, and T. Dirgantara, ChemistrySelect 8 (2023) 3023.
[21] A.K. Ayal, Z. Zainal, A.M. Holi, H.N. Lim, Z.A. Talib, and Y.C. Lim, J. Phys. Chem. Solids. 153 (2021) 110006.
[22] K. Chahrour, F.K. Yam, M. K.M. Chahrour, and M.R. Hashim, Mater. Lett. 273 (2020) 127922.
[23] H.K. Abd El-Hamid, A.A. Gaber, Rehab E. A. Ngida, H.E.H. Sadek, R.M. Khattab, and H.S. Mandour, Scientific Reports 14 (2024) 68566.

[24] A. L. Cuevas, A. Domínguez, J. Zamudio-García, V. Vega, A. S. González, D. Marrero-López, V. M. Prida, and J. Benavente, Materials 17 (2024) 1412.
[25] L. Bouchama, N. Azzouz, N. Boukmouche, J.P. Chopart, A.L Daltin, and Y. Bouznit, Surf. Coat. Technol. 235 (2013) 676.
[26] B.D. Cullity, and S.R. Stock, Elements of X-Ray Diffraction. Third ed, Prentice-Hall Inc, New York (2001).
[27] M. Wilke, G. Teichert, and R. Gemma, Thin Solid Films. 520 (2011) 1660.
[28] T. Nelis, and R. Payling, Anal. Bioanal. Chem. 382 (2005) 863.
[29] H. Kou, X. Zhang, Y. Du, W. Ye, Sh. Lin, and C. Wang, Appl. Surf. Sci. 257 (2011) 4643.
[30] J. Lee, Y. Yun, J. Oh, and Y. Tak, Electrochim. Acta 51 (2005) 1.
[31] M. Izaki, and T. Omi, J Electrochem Soc. 143 (1996) L53.
[32] B.Q. Cao, W.P. Cai, F.Q. Sun, Y. Li, Y. Lei, and L.D. Zhang, Chem. Commun. 14 (2004) 1604.
[33] O. Kerivel, Dopage des films minces de ZnO:étude de l'insertiond' Al par spectroscopied' absorption X et de l'interaction du Mg avec des couches ultra-minces épitaxiées sur Ag(111), Doctoral thesis, Sorbonne University (2023).
[34] I. MiroI, C. Enache, and I. Grozescu, Dig. J. Nanomater. Biostruct. 7 (2012) 967.
[35] X. Wei, and D. Chen, Mater. Lett. 60 (2006) 823.
[36] S. Mohamed, Nanomaterials 13 (2023) 2667.
[37] C. Lupan, N. Kohlmann, D. Petersen, M. T. Bodduluri, A. Buzdugan, J. Jetter, E. Quandt, L. Kienle, R. Adelung, and O. Lupan, Materials Today Nano 29 (2025) 100596.
[38] J. Oh, and C.V. Thompson, Electrochim. Acta 56 (2011) 3731.
[39] G. Patermarakis, and K. Moussoutzanis, J. Electroanal. Chem. 659 (2011) 176.
[40] C. Xiao, T. Yang, M. Chuai, B. Xiaoa, and M. Zhang, Chem. Phys. 18 (2016) 325.
[41] A. Umar, and Y.B. Hahn, Nanotechnol. 17 (2006) 2174.
[42] V. Moutarlier, M.P. Gigandet, L. Ricq, and J. Pagetti, Appl. Surf. Sci. 183 (2001) 1.
[43] T.P. Hoar, and G.C. Wood, Electrochim. Acta 7 (1962) 333.
[44] J. Hitzig, K. Juttner, W.J. Lorentz, and W. Paatsch, Corros. Sci. 24 (1984) 945.
[45] J. Hitzig, K. Juttner, and W.J. Lorentz, J. Electrochem. Soc. 133 (1986) 887.
[46] J.J. Suay, E. Gimenez, T. Rodriguez, K. Habbib, and J.J. Saura, Corros. Sci. 45 (2003) 611.
[47] F. Mansfeld, G. Zhang, and C. Chen, Mater. Corros. 58 (2007) 825.
[48] Lv. Lihua, Z. Wang, X. Cao, and J. Han, Ceram. Inter. 51 (2025) 32950.
[49] L. Bouchama, Y. Bouznit, N. Boukmouche, and S. Irki, Anal. Bioanal. Electrochem.15 (2023) 264.
[50] T. Zhang, Z. Zheng, Z. Jiang, H. Yu, R. Ma, A. Du, Y. Fan, X. Zhao, and C. Li, Ceram. Inter. 51 (2025) 10143.

[51] W. He, Y. Liu, Y. Jia, Y. Zhao, and H. Le, Composites Communications 51 (2024) 102110.